Climate Dynamics (2026) 64:151
https://doi.org/10.1007/s00382-026-08118-y

ORIGINAL ARTICLE

Potential predictability of global seasonal precipitation anomalies determined by climate modes

Yu Wang[1] · Xiu-Qun Yang[1] · Dejian Yang[2] · Lingfeng Tao[3] · Jiabei Fang[1] · Xuguang Sun[1]

Received: 6 January 2026 / Accepted: 13 February 2026

Abstract
Accurate prediction of global seasonal precipitation anomalies (GSPA) is essential for mitigating flood and drought risks worldwide. However, current climate models exhibit limited skill in predicting GSPA, particularly in extratropical regions. While climate modes are acknowledged as major sources of predictability for GSPA, their specific contributions remain unclear. In this study, we first identify leading climate modes from tropical outgoing longwave radiation anomalies and extratropical 500 hPa geopotential height anomalies using EOF decomposition. We then develop a framework to independently reconstruct GSPA based on these modes, applying a 30-year sliding temporal window. By calculating the temporal correlation coefficient between the reconstructed and observed precipitation anomalies at each grid point, we quantitatively assess the potential predictability of GSPA using an optimal combination of climate modes for each season. Our results show that high potential predictability exists not only in the tropics where the leading mode associated with ENSO dominates, but also across various extratropical regions, especially in winter hemispheres, where the leading mode such as NAO or AAO plays a major role. The potential predictability derived here represents an upper limit achievable if these climate modes are perfectly predicted. Nevertheless, state-of-the-art coupled general circulation models (CGCMs) show clear deficiencies in predicting extratropical seasonal precipitation, largely due to their limited skill in predicting extratropical climate modes. This highlights that improving CGCMs' prediction of extratropical climate modes is crucial for advancing seasonal precipitation prediction in extratropical regions.

Keywords Climate predictability · Climate modes · Seasonal precipitation anomalies · Climate prediction · Coupled climate model

1 Introduction

Increasing risks of extreme climate disasters due to global warming has become a major challenge for global security and development. Among those, droughts and floods are the most frequent natural disasters, causing great loss of life and property. Many regions around the world frequently experience seasonal droughts or floods, such as the record-breaking flood during the summer of 2020 and the persistent drought during the summer of 2022 in the Yangtze River basin of China (Zhou et al. 2021; Ma et al. 2022; Zhang et al. 2024), the high-temperature droughts spanning Western Europe and North Africa during the spring of 2023 (Perkins-Kirkpatrick et al. 2024; Ionita et al. 2025), the extreme precipitation events in multiple European countries during the summer of 2024 (Zhang et al. 2025), and the severe wildfires in the western United States recently caused by persistent drought conditions (Kelley et al. 2025). Severe floods or persistent droughts are particularly extraordinary in global monsoon areas where climate variations are intensified with global warming (Gemenne et al. 2014). These climate disasters resulting from seasonal precipitation anomalies have caused profound impacts on human safety, agricultural production, energy security, and social order in the affected regions. To effectively prepare for these

✉ Xiu-Qun Yang
xqyang@nju.edu.cn

[1] China Meteorological Administration Key Laboratory for Climate Prediction Studies, School of Atmospheric Sciences, Nanjing University, Nanjing 210023, China

[2] College of Oceanography, Hohai University, Nanjing, China

[3] School of Atmospheric Sciences, Nanjing University of Information Science and Technology, Nanjing, China

Published online: 16 March 2026

extreme drought and flood events, accurate seasonal precipitation predictions are crucial for informed decision-making.

In seasonal climate prediction, Coupled general circulation models (CGCMs) are important tools developed in major national meteorological agencies worldwide, such as the eight CGCMs used for seasonal forecasts in the Copernicus Climate Change Service (C3S) (Giuntoli et al. 2022; O'Reilly et al. 2025). Previous studies indicated that multimodel ensemble (MME) can substantially enhance the reliability of seasonal prediction skills (Lee et al. 2010; Yang et al. 2018, 2021, 2023). However, due to chaotic feature of the atmosphere, CGCMs with various uncertainties in initial conditions, parameterizations of physical processes, and numerical algorithms practically exhibit limited skills in seasonal precipitation prediction particularly over the mid-to-high latitude regions (Yang et al. 2016, 2018; Mishra et al. 2018; Roy et al. 2020).

A variety of previous studies demonstrated that large-scale climate modes play a pivotal role in shaping global seasonal precipitation anomalies and serve as primary sources of seasonal precipitation predictability (Palmer and Anderson 1994; Yang et al. 1998; Doblas-Reyes et al. 2013; Le et al. 2023). Among those, El Niño/Southern Oscillation (ENSO) as the strongest signal of climate system is the dominant tropical climate mode affecting seasonal precipitation anomalies in many regions of globe through teleconnections (Ropelewski and Halpert 1987; Dai et al. 1997; Lyon and Barnston 2005; Shaman 2014; Sun et al. 2021). For instance, ENSO events which generally mature in winter can simultaneously cause wintertime precipitation anomalies in North America through the Pacific/North American (PNA) teleconnection (Straus and Shukla 2002; Liu et al. 2011), acting as a far-reaching effect in the extratropics. Also, a warm ENSO event (El Niño) tends to induce a persistent anomalous western Pacific anticyclone through the Indian Ocean capacitor effect (Xie et al. 2009; Li et al. 2017), thereby causing a severe following summer flood in subtropical East Asia (Xie et al. 2016; Chowdary et al. 2019; Sun et al. 2021). The Indian Ocean Dipole (IOD) emerges as another critical tropical climate mode which can significantly affect precipitation anomalies in South Asia and the Arabian Peninsula by perturbing the South Asian monsoon system (Saji et al. 1999; Abram et al. 2008; Yuan et al. 2008). Besides the tropical climate modes, extratropical climate modes such as the North Atlantic Oscillation (NAO) and the Arctic Oscillation (AO) can also exert substantial impacts on regional precipitation variabilities (Hurrell and Deser 2009; Casanueva et al. 2014; He et al. 2017). For instance, NAO tends to affect winter precipitation across Europe by modulating the intensity and position of westerly jet stream (Seager et al. 2020), while AO tends to induce summer precipitation anomalies characterized by a tripolar pattern in East Asia through a Eurasian teleconnection (Enomoto et al. 2003; Gong and Ho 2003).

It is noteworthy that the sources of seasonal precipitation predictability do not merely rely on a single climate mode, but on the synergistic effects of multiple climate modes (Wang et al. 2015; Hobeichi et al. 2024). For instance, when El Niño co-occurs with a positive phase of IOD, sea surface temperature (SST) anomalies are characterized by a tripolar distribution across the equatorial Indo-Pacific region, which can amplify ENSO's impacts on global precipitation (Nguyen-Le et al. 2024). A notable example occurred in 1997/98 when positive phases of ENSO and IOD are combined, which caused a catastrophic following summer flood in East Asia (Ashok et al. 2001; Weng et al. 2011; Qiu et al. 2014). ENSO also demonstrates synergistic impacts with extratropical climate modes. It was showed that phase alignment between ENSO and PDO (the Pacific Decadal Oscillation) can amplify precipitation anomalies along North America's western coast (Goodrich 2007; Zhu et al. 2008). Furthermore, during positive phases of ENSO, negative phases of NAO tend to induce northward shifts of the East Asian subtropical jet and southward displacements of the polar front jet (Wu et al. 2009a, b). Simultaneously, an anomalous cyclonic circulation emerges in the mid-lower troposphere between Lake Balkhash and Lake Baikal, facilitating the convergence of cold and warm air masses over northern China and leading to increased snowfall in that region (Liu et al. 2023; Zhou et al. 2025).

From the perspective of predictability, seasonal precipitation anomalies can be basically decomposed into predictable components determined by climate modes and unpredictable ones determined by chaotic variabilities (Yang et al. 1998; Hassan et al. 2004). Potential predictability of seasonal precipitation anomalies is fundamentally determined by climate modes, but actual predictability of seasonal precipitation anomalies depends on how accurately those climate modes are predicted. Thus, it is crucial to investigate the potential predictability of global seasonal precipitation anomalies determined by climate modes, since this may give us an upper limit achievable of the predictability as the climate modes are perfectly predicted. Such an investigation also has practical value for encouraging operational agencies to improve their predictions of major climate modes with CGCMs in order to eventually advance their predictions of global seasonal precipitation anomalies. However, previous studies on the investigation exhibit some limitations. First, previous studies predominantly focused on the regional impacts of individual climate modes such as ENSO. There remains a lack of comprehensive, global-scale analyses, particularly regarding the influence of extratropical climate modes on global precipitation anomalies. The synergistic effects of tropical and extratropical climate

modes on global precipitation variabilities have not been well explored. Second, methodological gaps exist in quantifying predictability contributions. Many studies rely solely on model evaluations and comparisons to assess prediction performance, thereby providing only indirect assessments of predictability (Hausfather et al. 2020). Crucially, those studies have not explicitly isolated or quantitatively delineated the actual contributions of distinct climate modes to the global precipitation predictability. Third, a fundamental gap remains in systematically quantifying the upper limit of seasonal precipitation predictability determined by climate modes. If the states of all key climate modes are known in advance, what is the maximum predictability of global seasonal precipitation? What are the relative contributions of different climate modes to the predictability? These unresolved questions highlight major concerns in understanding the predictability of global seasonal precipitation anomalies.

In this study, we first identify dominant tropical and extratropical climate modes influencing global seasonal precipitation anomalies with empirical orthogonal function (EOF) decomposition of two representative variables. We then independently reconstruct global seasonal precipitation anomalies using an optimal combination of those climate modes with multiple linear regression, enabling a quantitative assessment of potential predictability of global seasonal precipitation anomalies determined by those climate modes and an analysis compared with the CGCM prediction skills. Further, we quantify the contributions of leading climate modes to the precipitation predictability. The rest of the paper is organized as follows. Section 2 describes data and methods employed in this study. Section 3 identifies leading climate modes and their interdecadal changes. Section 4 investigates potential predictability of global seasonal precipitation anomalies determined by those climate modes, with a comparison with the predictive skills of current CGCMs. Section 5 presents a quantitative assessment of contributions of leading climate modes to the potential predictability. Final section is devoted to summary.

2 Data and methods

2.1 Data

This study utilizes the ERA5 (Hersbach et al. 2020) monthly reanalysis dataset from the European Centre for Medium-Range Weather Forecasts (ECMWF) to characterize large-scale atmospheric circulation, including outgoing longwave radiation (OLR) and geopotential height at 500 hPa (Z500). To enable the reconstruction of precipitation anomalies over an extended time span and facilitate a robust assessment of their potential predictability, this study utilizes monthly precipitation data from the ERA5 reanalysis dataset. In addition, SST data is also taken from ERA5. Given the original spatial resolution of 0.25° longitude and 0.25° latitude in ERA5, all variables are bilinearly interpolated into a uniform 1° longitude and 1° latitude grid to focus on large-scale circulation patterns and their relationships with precipitation and SST anomalies. The season definition follows standard meteorological convention, that is, spring (March–April–May average, MAM), summer (June–July–August average, JJA), autumn (September–October–November average, SON), and winter (December-January–February average, DJF). The climatological reference period is defined as 30 years, and the time span for all the data is for 1951–2023 (73 years in total).

To compare the potential predictability of global seasonal precipitation anomalies obtained from the observation with that from CGCMs, this study employs hindcast outputs from 8 state-of-the-art CGCMs released by the Copernicus Climate Change Service (C3S) (Buontempo et al. 2022). These models are utilized to assess CGCMs' predictive skills for global seasonal precipitation anomalies through cross-seasonal prediction experiments. Cross-seasonal predictions are defined as forecasts initialized three months prior to the target season (e.g., the summer predictions generated from initial conditions of March). The hindcast period spans 1994–2016, with all models configured at a uniform horizontal resolution of 1° longitude and 1° latitude.

Additionally, to characterize some of the leading climate modes, we incorporate multiple climate indices, including those of the Nino3.4, AO, NAO, the East Atlantic (EA) pattern, the West Pacific (WP) pattern, the Pacific–North American (PNA) pattern, the East Atlantic/West Russian (EA/WR) pattern, the Scandinavian (SCA) pattern, and the Antarctic Oscillation (AAO). All of the indices are obtained from the National Oceanic and Atmospheric Administration (NOAA) Physical Sciences Laboratory.

2.2 Methods

We employ EOF decomposition to identify large-scale climate modes from anomalous circulation fields of OLR in the tropics (30°N–30°S) and Z500 (30°N–90°N and 30°S–90°S) in the extratropics. Before the EOF decomposition, linear trends are removed from all circulation fields, and the influence of ENSO is eliminated from the Z500 data through linear regression. To investigate the potential predictability of global seasonal precipitation anomalies determined by climate modes, we apply multiple linear regression to independently reconstruct seasonal precipitation anomalies in terms of the identified climate modes, which is detailed in Sect. 4. An uncentered temporal correlation coefficient

(TCC) is calculated to measure seasonal precipitation predictability at each grid point, which is written as,

$$TCC\,(s) = \frac{\sum_{t=1}^{N} o(s,t) f(s,t)}{\sqrt{\sum_{t=1}^{N} (o(s,t))^2}\sqrt{\sum_{t=1}^{N} (f(s,t))^2}}, \quad (1)$$

where N represents the length of time series. The terms $o\,(s,t)$ and $f\,(s,t)$ stand for the observed and reconstructed (or CGCM-predicted) seasonal precipitation anomalies at each grid point (s) for each year (t), respectively.

3 Leading climate modes and their interdecadal changes

Large-scale climate modes are the primary sources of global seasonal precipitation predictability. In general, these climate modes can be categorized into two types: tropical and extratropical climate modes. The tropical climate modes such as ENSO and IOD are mostly the consequences of large-scale air-sea interactions, which manifest as anomalous SSTs in the ocean and anomalous convection activities in the atmosphere, particularly in the Indo-Pacific warm pool. Anomalous tropical convection activities accompany anomalous latent heat releases which can directly cause atmospheric circulation and precipitation anomalies not only in the tropics but also in the extratropics through teleconnections. Thus, we here simply use OLR fields which indicate convection activities (rather than SST fields) in the tropics (30°N–30°S) to identify tropical climate modes with EOF decomposition.

Figure 1 shows the temporal evolutions and spatial distributions of the first EOF modes of tropical OLR anomalies, along with associated SST anomalies, during recent period of 1991–2021 for four seasons. It is well known that ENSO is the dominant climate mode in the tropics, which is clearly confirmed by the OLR-derived first modes as illustrated in Fig. 1. The first modes for four seasons comprehensively capture a complete life cycle of El Niño, including its initiation, development, maturity, and decay. Particularly, there occurred two extreme El Niño events in 1997/98 and

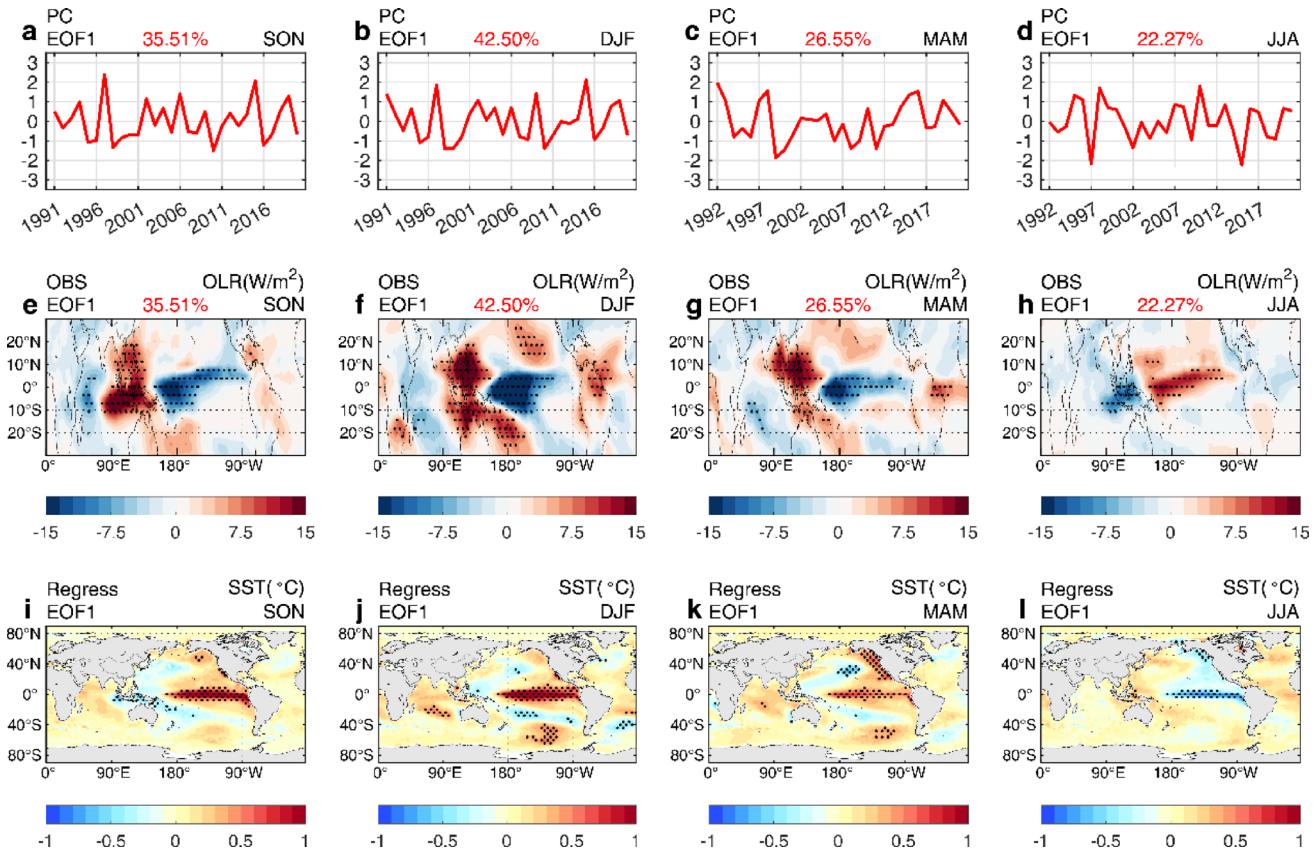

Fig. 1 Spatiotemporal characteristics of the leading tropical climate modes for four seasons identified with EOF decomposition from the OLR anomalies in the tropics (30°N–30°S) during recent period of 1991–2021. Panels from left to right are for SON (1991–2020), DJF (1991–2020), MAM (1992–2021), and JJA (1992–2021). Top panels **a**–**d** indicate standardized time series corresponding to the first EOFs, while middle panels **e**–**h** indicate spatial distributions of those EOFs for OLR anomalies (shading, unit: Wm^{-2}). Bottom panels **i**–**l** indicate the SST anomalies (shading, unit: °C) regressed upon those standardized time series in (a–d). Note that the areas with anomalies exceeding 95% confidence level with the Student's t-test are stippled

2015/16, as seen from their corresponding principal components (Fig. 1a–c). In SON, the first EOF captures El Niño at its developing phase, characterized by positive SST anomalies in the tropical eastern Pacific and negative SST anomalies in the maritime continent (Fig. 1i). This SST configuration tends to suppress convection over the maritime continent but enhance it over the equatorial central-to-western Pacific (Fig. 1e). In DJF, the first EOF exhibits El Niño at its mature phase, with the largest variance contribution of 42.5% among four seasons. During this season, positive SST anomalies in the tropical eastern Pacific are the largest (Fig. 1j), leading to active convection over the equatorial central-to-western Pacific and suppressed convection over the maritime continent (Fig. 1f). This configuration tends to give rise to increased precipitation in southeastern China and southeastern United States (as shown in Fig. 10h). In MAM, the first EOF just depicts El Niño at its decay phase, with anomalous SST and convection patterns similar to the situations during the proceeding winter, but with weakened amplitudes (Fig. 1k and 1g). In JJA, the first EOF displays El Niño at its transitional phase, characterized by a reversal of SST anomalies (Fig. 1l). This SST shift likewise induces a reversal of anomalous convection activities (Fig. 1h), which ultimately causes considerable precipitation increase in subtropical East Asia through anomalous western Pacific anticyclone (Li et al. 2017; Sun et al. 2021). Furthermore, it is found that the leading climate modes identified with tropical OLR anomalies reflect not only ENSO with SST anomalies in the tropical Pacific, but also convection and SST anomalies in/over the tropical Indian Ocean (Fig. 1h and 1l), suggesting a combined ENSO-IOD mode. Consequently, such a mode effectively encapsulates the primary characteristics of tropical convection variability. Therefore, utilizing tropical OLR anomalies to characterize major tropical climate modes provides an intuitive tool for investigating their contributions to the global seasonal precipitation predictability.

Unlike those tropical climate modes, extratropical climate modes such as NAO and AO may arise from compound effects of the SST, sea ice, and land surface variabilities as well as the atmospheric internal fluctuations. All of these effects can be reflected in the atmospheric circulation anomalies, which can be represented with Z500 anomalies, given their equivalent-barotropic vertical structures, geostrophic relations with wind anomalies, and hydrostatic relations with temperature anomalies Thus, we here simply use anomalous Z500 fields in the extratropics (90°N–30°N and 90°S–30°S) to identify extratropical climate modes both in the Northern Hemisphere and in the Southern Hemisphere with EOF decomposition.

Figure 2 shows the temporal evolutions and spatial distributions of the first EOF modes of Z500 anomalies in the extratropical Northern Hemisphere, along with associated SST anomalies, during recent period of 1991–2021 for four seasons. The leading extratropical climate modes in the Northern Hemisphere are the most prominent during DJF, as compared with other seasons. As shown in Fig. 2f, the first EOF mode of Z500 anomalies in the extratropical Northern Hemisphere exhibits an NAO pattern in DJF, characterized by negative anomalies over near Iceland, positive anomalies over near the Azores, and negative anomalies over across the Arctic. The Euro-Atlantic sector displays a pronounced north–south geopotential height gradient. Notably, positive anomalies are observed over Mongolia and the North Pacific. Concurrently, the North Atlantic SST exhibits a tripolar anomaly (NAT) pattern (Pan 2005; Chen et al. 2020), as seen in Fig. 2j. Particularly the noteworthy is the extremely strong negative phase of NAO mode occurred during DJF of 2009/10, as seen in Fig. 2b. In following MAM, the NAO mode tends to weaken substantially with negative anomaly center shifting westward (Fig. 2g). However, the NAT pattern of SST anomalies persists during MAM (Fig. 2k). In JJA, the NAO mode appears to the weakest, manifesting only as a weak negative anomaly center over the Arctic and a weak positive anomaly center over northwestern Europe (Fig. 2h), while the NAT pattern tends to diminish (Fig. 2l). In SON, the first EOF of Z500 anomalies features the Western Pacific (WP) pattern (Fig. 2e) with SST anomalies the most significantly in North Pacific (Fig. 2i), while the NAO pattern becomes insignificant. In summary, over the recent three decades, the NAO mode is the dominant climate mode in the extratropical Northern Hemisphere. By regulating the strength of the westerlies, the stability of the polar vortex, and the sea ice distribution, NAO can profoundly influence the climate of Europe, North America, and the Arctic, especially the seasonal precipitation anomalies across the extratropical Northern Hemisphere (as shown in the rightmost column of Fig. 12), providing one of the crucial extratropical sources of global seasonal precipitation predictability.

Figure 3 shows the temporal evolutions and spatial distributions of the first EOF modes of Z500 anomalies in the extratropical Southern Hemisphere, along with associated SST anomalies, during recent period of 1991–2021 for four seasons. It is clearly demonstrated in Fig. 3 that the leading EOFs in the extratropical Southern Hemisphere for all seasons are characterized by the Antarctic Oscillation (AAO) or the Southern Annular Mode (SAM), with variance contributions exceeding 30%. This feature indicates that AAO (or SAM) is the dominant climate mode in the extratropical Southern Hemisphere for any season, which is consistent with previous results (Gong and Wang 1999; Wu et al. 2009a, b). Spatially, this mode is characterized by negative geopotential height anomalies over the Antarctic region, surrounded by positive anomalies along the

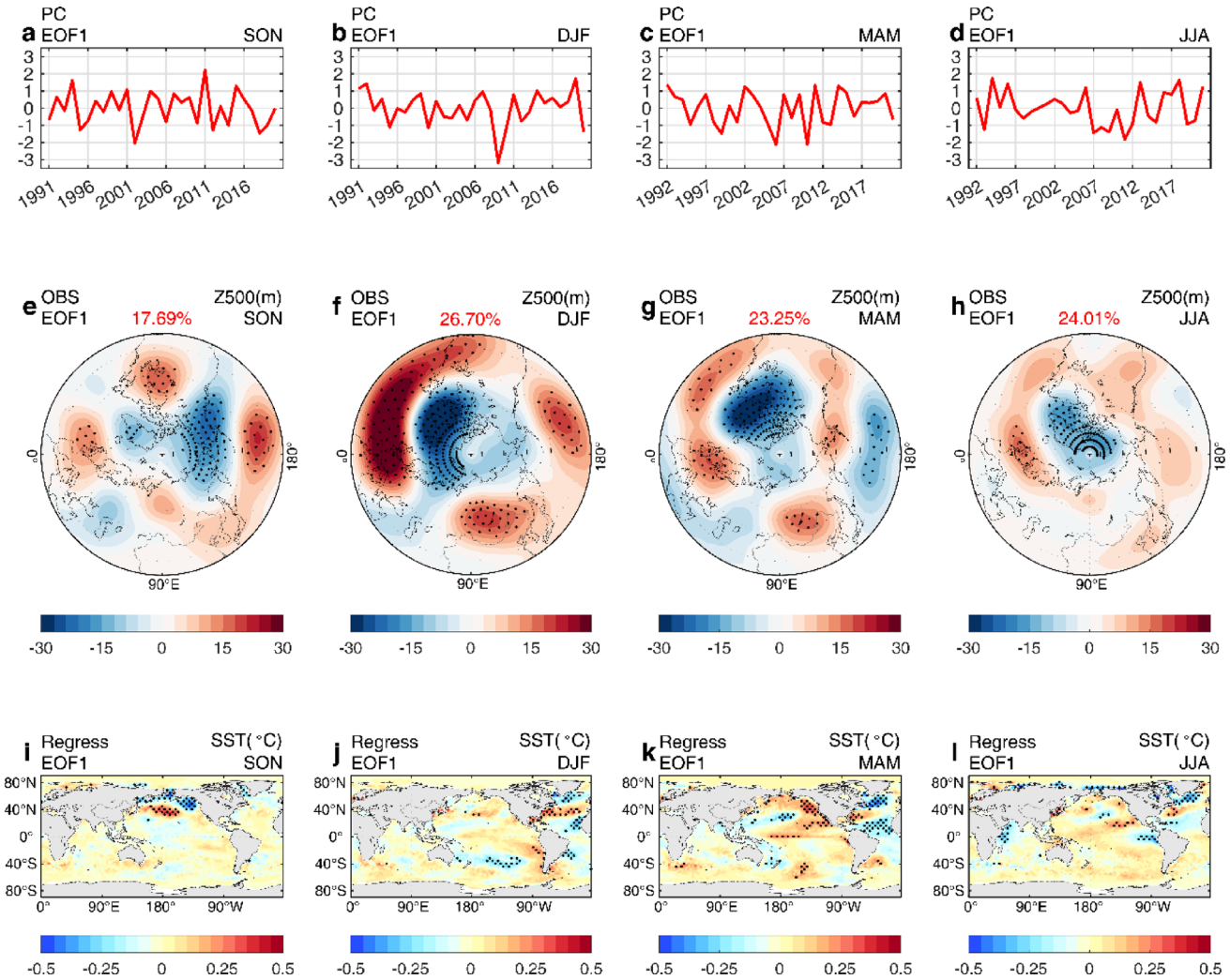

Fig. 2 Spatiotemporal characteristics of the leading extratropical Northern Hemisphere climate modes for four seasons identified with EOF decomposition from the Z500 anomalies north of 30°N during recent period of 1991–2021. Panels from left to right are for SON (1991–2020), DJF (1991–2020), MAM (1992–2021), and JJA (1992–2021). Top panels **a**–**d** indicate standardized time series corresponding to the first EOFs, while middle panels **e**–**h** indicate spatial distributions of those EOFs for Z500 anomalies (shading, unit: m). Bottom panels **i**–**l** indicate the SST anomalies (shading, unit: °C) regressed upon those standardized time series in (a–d). Note that the areas with anomalies exceeding 95% confidence level with the Student's *t*-test are stippled

circum-Antarctic belt. This climate mode appears to stronger during the austral winter (JJA), particularly over near the Antarctic Peninsula where enhanced sea ice cover induces a pronounced negative geopotential height anomaly center (Fig. 3h). During the austral summer (DJF), although the amplitude of the mode weakens slightly, its spatial structure remains clearly identifiable (Fig. 3f). During the transitional seasons (SON and MAM), the mode displays with moderate strength (Fig. 3e and g). The AAO mode can exert profound impacts on climate anomalies across the Southern Hemisphere. Beyond its direct influence on the Antarctic continent, it can significantly modulate seasonal precipitation patterns in southern Africa, Australia, and southern South America (Feng et al. 2010), suggesting the critical importance of the leading climate mode in determining global seasonal precipitation predictability (as shown in the right panel of Fig. 11).

Recent studies have suggested that some of those climate modes exhibit interdecadal changes, not only in their structures but in their dominance (Sun et al. 2021; Piskala and Huth 2025). So far, we have identified three leading climate modes, ENSO, NAO, and AAO, for the period of recent 30 years. Next, we examine if these leading modes have interdecadal changes by examining and comparing the first EOFs of tropical OLR anomalies and extratropical Z500 anomalies in DJF for three distinct interdecadal periods: 1951–1980, 1971–2000, and 1991–2020. Figure 4 demonstrates the first EOFs of tropical OLR anomalies and extratropical Southern Hemisphere Z500 anomalies for the three interdecadal periods. Overall, the tropical and extratropical

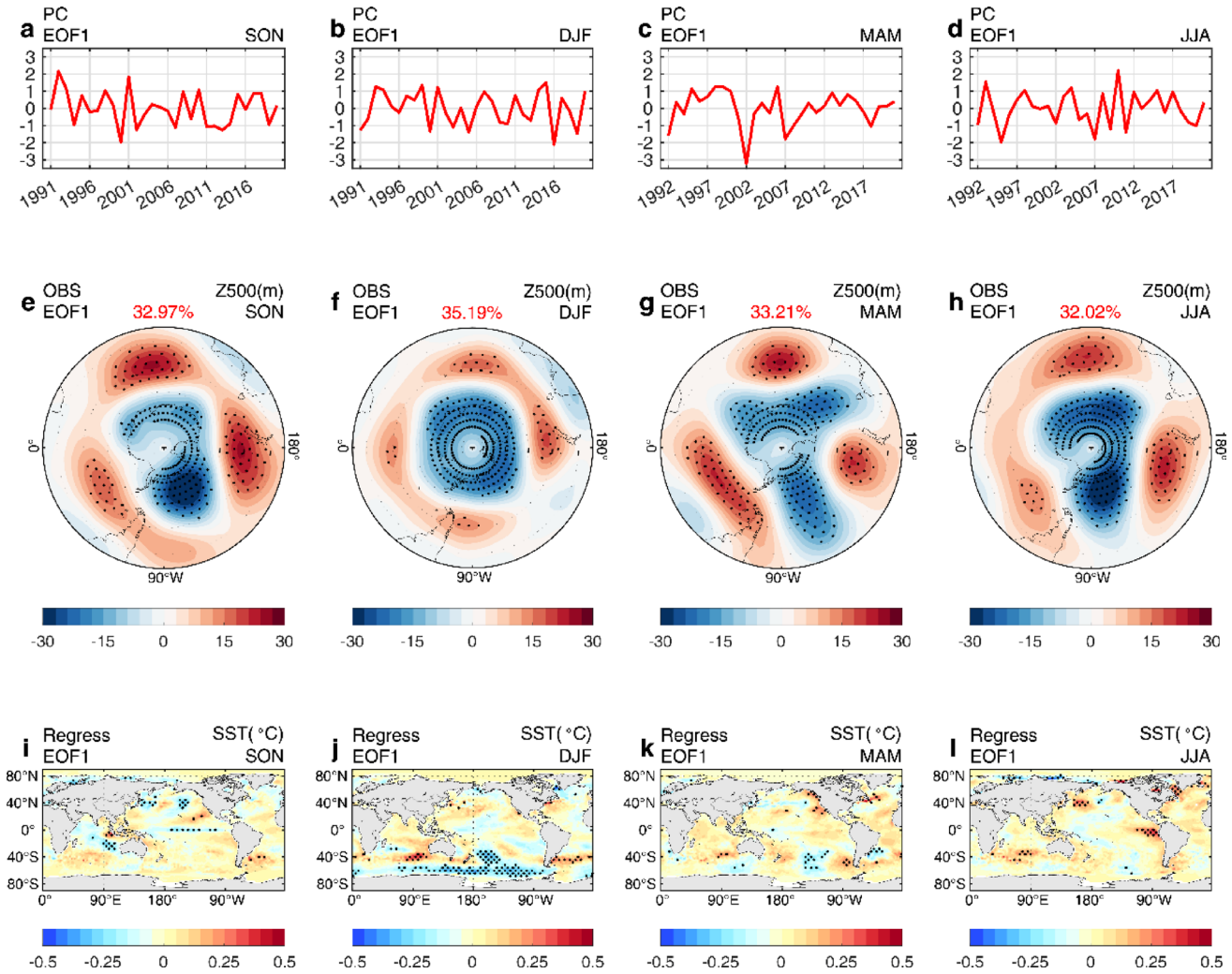

Fig. 3 As in Fig. 2, but for the leading extratropical Southern Hemisphere climate modes identified from Z500 anomalies south of 30°S

Southern Hemisphere leading modes remain unchanged across the three interdecadal periods. The first EOFs of the tropical OLR anomalies consistently exhibit the ENSO signature across all three periods (upper two panels of Fig. 4), maintaining a statistically significant high correlation with the Niño3.4 index. But notable spatial structure changes are observed. As compared to the 1951–1980 period (Fig. 4d), the latter two periods (1971–2000 and 1991–2020) (Fig. 4e and 4f) show more enhanced convection in the equatorial central-to-western Pacific and more suppressed convection over the Maritime Continent, which may be attributed to the interdecadal change in properties of ENSO events (Kim and Ha 2015). The first EOFs of the extratropical Southern Hemisphere Z500 anomalies consistently exhibit the AAO patterns across all three periods (lower two panels of Fig. 4), having a robust correlation with the AAO index. Changes of the leading modes in spatial structure are minor, including slight shifts in the locations of negative Z500 anomalies over the Antarctic and slight changes in the intensity of positive Z500 anomalies over the circum-Antarctic regions. Therefore, above unchanging features of the leading climate modes in the tropics and extratropical Southern Hemisphere will enable their robust contributions to seasonal precipitation predictability.

The interdecadal changes of the leading climate modes in the extratropical Northern Hemisphere are complex. Figure 5 shows the spatial characteristics of the first two EOFs of extratropical Northern Hemisphere Z500 anomalies in DJF for the three interdecadal periods. During the first period (1951–1980), the first EOF exhibits a PNA pattern (Fig. 5d) with a high correlation with PNA index (Fig. 5a), while the second EOF appears to be NAO (Fig. 5k) with a high correlation with NAO index (Fig. 5h). Both EOFs have relatively comparable variance contributions, indicating PNA and NAO are dominant extratropical Northern Hemisphere climate modes during the earlier interdecadal peiod. However, during the second period (1971–2000), the first two EOFs appear to be combined PNA-NAO modes with

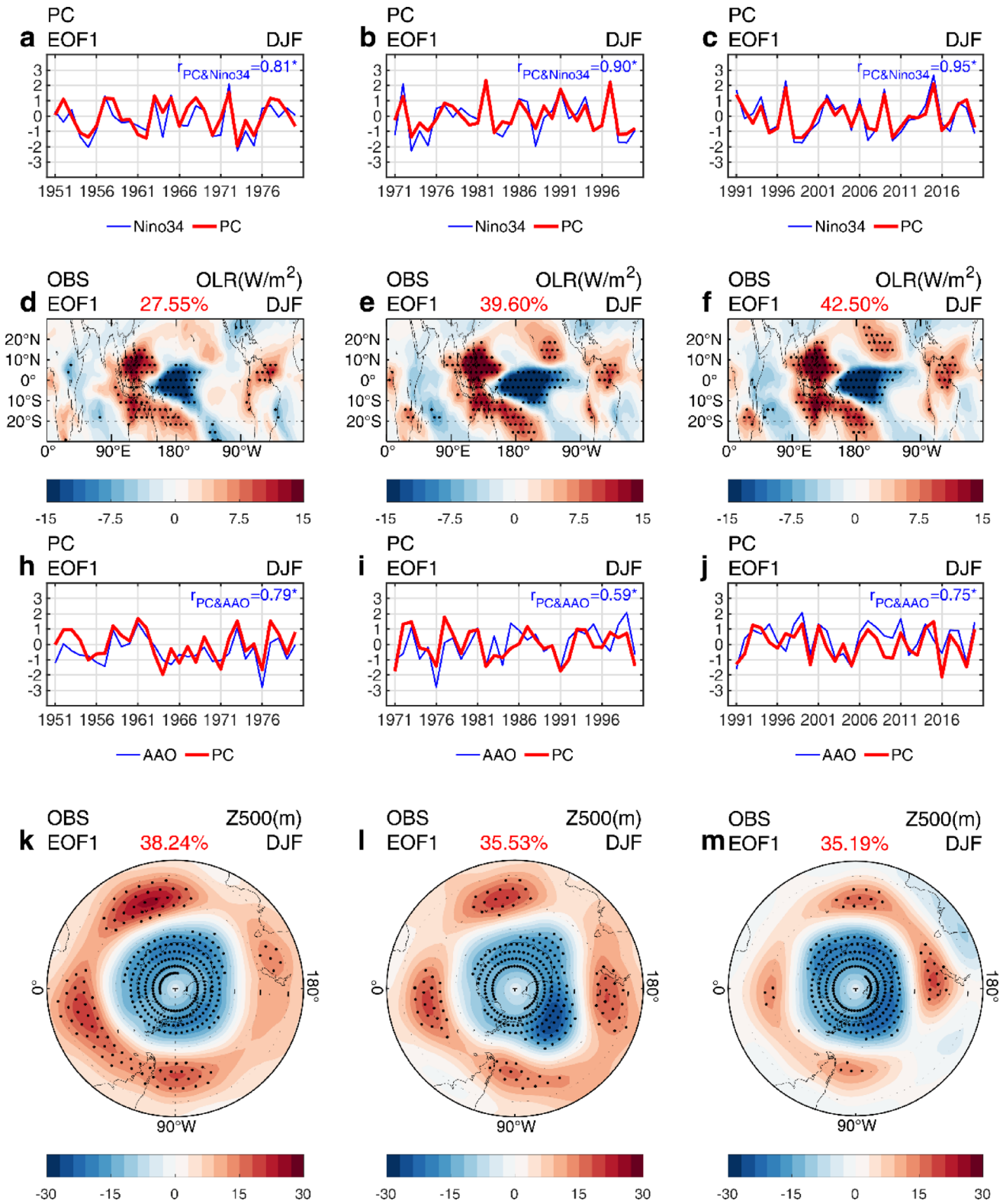

Fig. 4 Spatiotemporal characteristics of the leading climate modes identified with EOF decomposition from the tropical (30°N–30°S) OLR anomalies and the extratropical Southern Hemisphere (south of 30°S) Z500 anomalies during DJF for the interdecadal periods of 1951–1980, 1971–2000, and 1991–2020 (from left to right). Upper two panels show the standardized time series (PCs) of the first EOFs of the OLR anomalies, along with the Niño3.4 index **a**–**c**, and the spatial distributions of the EOFs **d**–**f**. Lower two panels present the standardized time series (PCs) of the first EOFs of the Z500 anomalies, together with the AAO index **g**–**i**, and the spatial distribution of the EOFs **k**–**m**. Note that the areas with anomalies and the correlation coefficients between the PCs and the indices exceeding 95% confidence level with the Student's *t*-test are stippled and star-marked, respectively

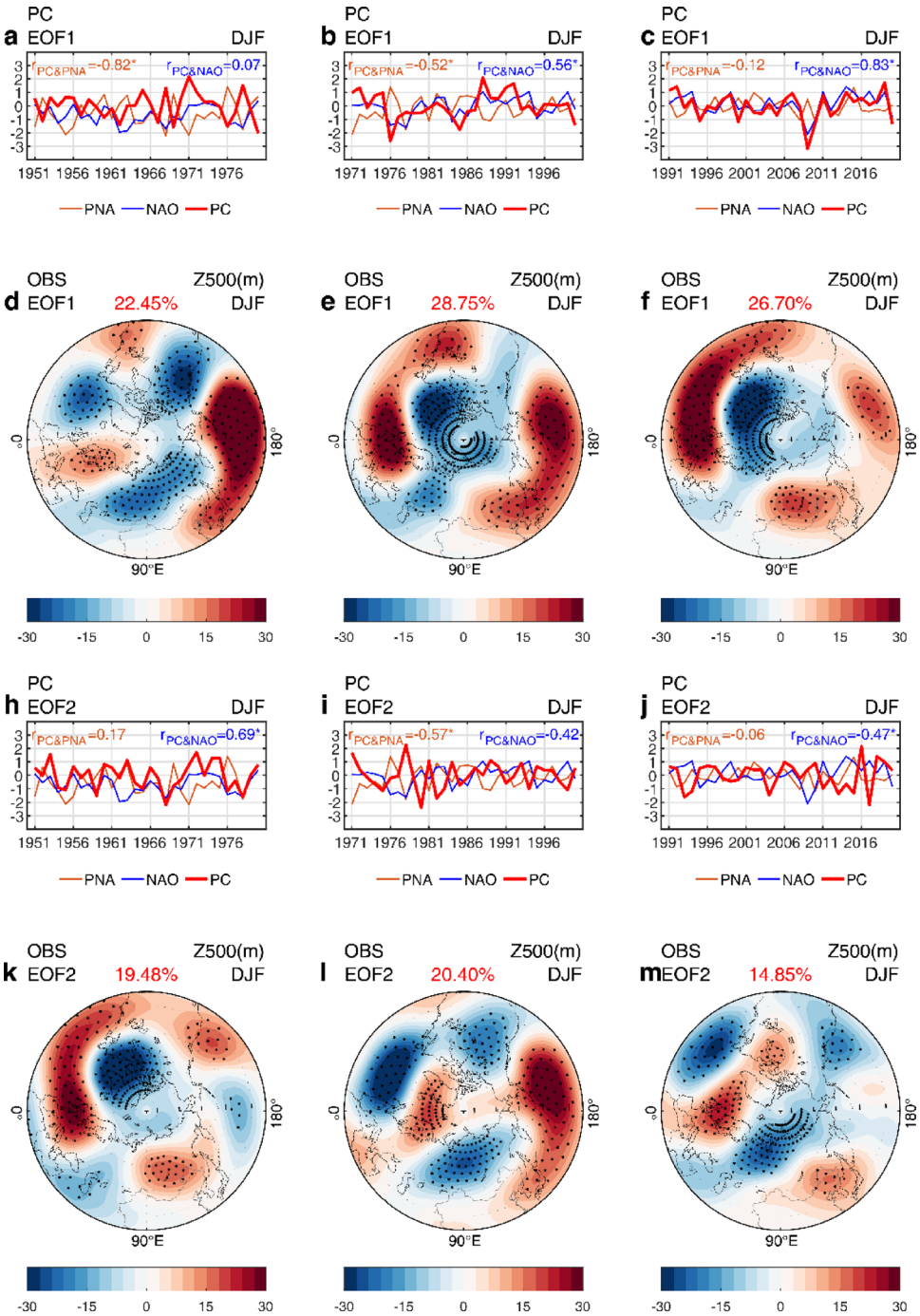

Fig. 5 Spatiotemporal characteristics of the leading climate modes identified with EOF decomposition from the extratropical Northern Hemisphere (north of 30°N) Z500 anomalies during DJF for the interdecadal periods of 1951–1980, 1971–2000, and 1991–2020 (from left to right). Upper two panels show the standardized time series (PCs) of the first EOFs of the Z500 anomalies, along with the PNA and NAO indices **a**–**c**, and the spatial distributions of the EOFs **d**–**f**. Lower two panels are the same as in upper panels, but for the second EOFs. Note that the areas with anomalies and the correlation coefficients between the PCs and the indices exceeding 95% confidence level with the Student's *t*-test are stippled and star-marked, respectively

the first EOF being more NAO-like (Fig. 5b and 5e) and the second EOF being more PNA-like (Fig. 5i and 5l). During the third peiod (1991–2020), the first EOF features completely a NAO pattern (Fig. 5f) with a high correlation with NAO index (Fig. 5c), whereas the second EOF no longer resembles the PNA pattern, but instead manifests as a zonal wave train extending from the North Atlantic through northern Europe and Siberia to Northeast Asia (Fig. 5j and 5m). Further, we calculate the correlation coefficients between the first three EOFs and the indices of seven conventional climate modes for the three interdecadal periods, as listed in Table 1. It can be seen that overall each of the first three EOFs derived from extratropical Northern Hemisphere Z500 anomalies can respectively reflect one of the conventional modes in the wintertime extratropical Northern Hemisphere, except for the second period when the EOFs exhibit types of combinations of multiple conventional modes. This suggests that, unlike those in the tropics and extratropical Southern Hemisphere, the leading climate modes in the extratropical Northern Hemisphere have undergone

Table 1 Correlation coefficients between the standardized time series (PCs) of the first three EOFs of the extratropical Northern Hemisphere Z500 anomalies during DJF for three interdecadal periods and the seven major conventional climate mode indices

	1951–1980			1971–2000			1991–2020		
	EOF1	EOF2	EOF3	EOF1	EOF2	EOF3	EOF1	EOF2	EOF3
AO	0.33	0.35	0.12	**0.75***	−0.29	0.14	**0.78***	−0.16	0.06
NAO	0.07	**0.69***	0.33	**0.56***	**−0.42***	**0.49***	**0.83***	**−0.47***	0.01
EA	0.28	−0.27	0.13	−0.23	**0.48***	0.14	−0.09	0.05	−0.15
WP	0.36	−0.05	**0.40***	0.22	**0.37***	−0.16	0.10	0.22	**0.39***
PNA	**−0.82***	0.17	0.20	**−0.52***	**−0.57***	0.05	−0.12	−0.06	**0.44***
EAWR	0.29	**0.54***	−0.18	**0.63***	0.03	**−0.45***	**0.38***	**0.62***	0.03
SCA	**0.37***	−0.16	**0.50***	**−0.44***	**0.42***	0.10	**−0.70***	−0.12	−0.05

Note that the correlation coefficients exceeding 95% confidence level with the Student's *t*-test are in bold and star-marked

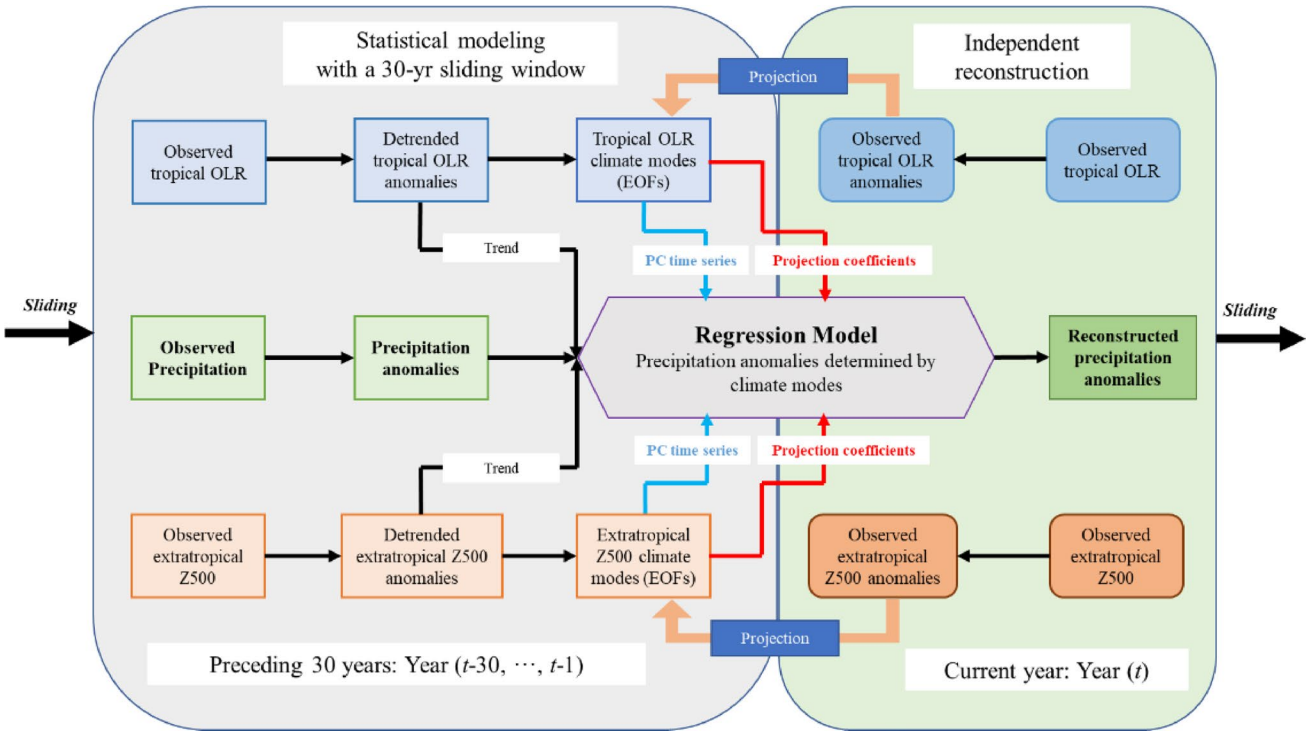

Fig. 6 Flowchart of a framework proposed for independently reconstructing global seasonal precipitation anomalies using climate modes with a 30-yr sliding temporal window

significant interdecadal changes both in their characteristics and in their relative contributions to climate variability.

4 Potential predictability of global seasonal precipitation anomalies

As predictable components of seasonal precipitation anomalies are determined by large-scale climate modes, it is interesting to reconstruct those precipitation anomalies using the climate modes and further examine how much the reconstructed precipitation anomalies can account for the original precipitation anomalies, i.e., the potential predictability of seasonal precipitation anomalies. In the last section, we have identified the leading climate modes both in the tropics and in the extratropics with EOF decomposition with respect to two representative variables: OLR and Z500 anomalies and found that the leading modes can have interdecadal changes. Here we develop a framework to independently reconstruct global seasonal precipitation anomalies using those identified climate modes, with a 30-yr sliding temporal window to consider interdecadal changes of climate modes due to the modulation of background state change. Detailed procedures of the framework illustrated in Fig. 6 are as follows. First, after removing long-term trends in all the variables and ENSO signature in the extratropical variables, we use observed tropical (30°N ~ 30°S) OLR anomalies and extratropical Northern (north of 30°N) and Southern (south of 30°S) Hemisphere Z500 anomalies to identify large-scale climate modes with EOF decomposition

for a 30-yr temporal window. Second, we construct a statistical model with multiple linear regression to quantify the relationship between the global seasonal precipitation anomalies at each grid point and the identified tropical (*OLR*), extratropical Northern Hemisphere (*Z500N*), and extratropical Southern Hemisphere (*Z500S*) climate modes, for the 30-yr temporal window, which is expressed as,

$$P = \sum_{i=1}^{M} \alpha_i * PC_i^{OLR} + \sum_{i=1}^{N} \alpha_j * PC_j^{Z500N} + \sum_{i=1}^{K} \alpha_k * PC_k^{Z500S} + PC^{trend} \quad (2)$$

where P denotes the seasonal precipitation anomalies, PC the standardized time series of each climate modes and trend, and α the coefficients regressed upon PC of each climate mode. M denotes the number of tropical climate modes, N the number of extratropical Northern Hemisphere climate modes, and K the number of extratropical Southern Hemisphere climate modes. Third, in terms of the statistical regression model (2), we independently reconstruct global seasonal precipitation anomalies at each grid point in the year (t) just after the 30-yr window ($t-30$, …, $t-1$), by projecting observed tropical OLR anomalies and extratropical Z500 anomalies in the year onto the climate modes (EOFs) used in (2), getting the projected coefficients (PCs) and then substituting them into the regression model (2), which is written as,

$$P(t) = \sum_{i=1}^{M} \alpha_i * \widehat{PC_i^{OLR}}(t) + \sum_{i=1}^{N} \alpha_j * \widehat{PC_j^{Z500N}}(t) + \sum_{i=1}^{K} \alpha_k * \widehat{PC_k^{Z500S}}(t) + PC^{trend} \quad (3)$$

where the formula is the same as (2), but for $P(t)$ denoting the reconstructed precipitation anomalies in the target year (t), $\widehat{PC}$ the projection coefficients upon each climate mode in the year. Through repeating above procedures with a 30-yr moving window, we can independently reconstruct global seasonal precipitation anomalies for 1981–2023 using climate modes.

However, we must point out that there is a challenge, that is, how we select climate modes to guarantee we can at utmost independently reconstruct the predictable components of global seasonal precipitation anomalies in terms of Eqs. (2) and (3). We test various combinations of climate modes (EOFs), trying to yield an optimal reconstruction. Considering the effective degrees of freedom in the regression models, for each grid point and each season in each year, there are 3276 possible combinations in total. We calculate the temporal correlation coefficient (TCC) between independently-reconstructed and observed seasonal precipitation anomalies at each grid point for all combinations and then use the globally-averaged TCC to serve as a metric to identify the optimal reconstruction. Figure 7 ranks the globally-averaged TCC across all combinations, from which we find an optimal combination of the leading climate modes with maximum globally-averaged TCC (up to 0.3 or larger) for each season as follows: 6 tropical modes, 3 Northern Hemisphere modes, and 3 Southern Hemisphere modes for MAM; 8 tropical modes, 1 Northern Hemisphere mode, and 6 Southern Hemisphere modes for JJA; 2 tropical modes, 6 Northern Hemisphere modes, and 6 Southern Hemisphere modes for SON; 3 tropical modes, 6 Northern Hemisphere modes, and 2 Southern Hemisphere modes for DJF. The seasonal differences in the optimal climate mode combinations may reflect different dominance of leading climate modes in seasonal precipitation anomalies. For example, the tropical climate modes (e.g., ENSO) are weaker in spring

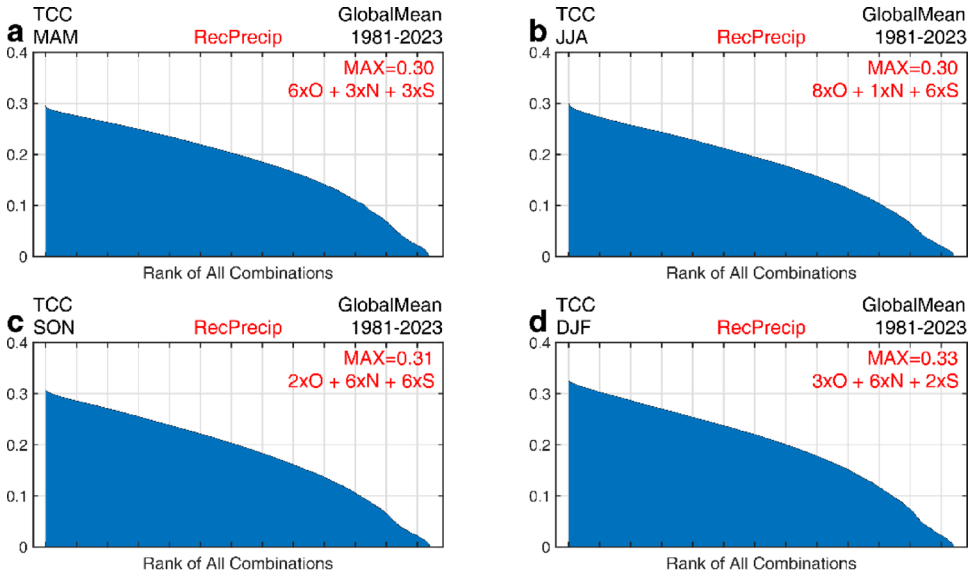

Fig. 7 Globally-averaged temporal correlation coefficients (TCCs) between independently-reconstructed and observed seasonal precipitation anomalies for 1981–2023 ranking in a descending order, plotted as a function of all combinations of the leading climate modes, for **a** MAM, **b** JJA, **c** SON, and **d** DJF. Detailed information of the combinations with maximum globally-averaged TCC are noted at the upper right corner of each panel

and summer, which necessitates the inclusion of more tropical modes to maximize the predictability, while those modes (e.g., ENSO) are stronger and fewer in autumn and winter, which makes their predictive powers dominant.

Figure 8 shows spatial distributions for four seasons of TCCs between the independently-reconstructed seasonal precipitation anomalies with the optimal combinations of climate modes and the observed seasonal precipitation anomalies. Obviously, these distributions represent the potential predictability of global seasonal precipitation anomalies determined by climate modes. Overall, high predictability appears to be in some of the tropical regions, particularly in tropical Pacific where ENSO dominates, which is consistent with previous results (Yang et al. 1998; Jan van Oldenborgh et al. 2005; Doblas-Reyes et al. 2013; Yang et al. 2016; Yang et al. 2018). It is striking that the climate modes-determined high predictability also exists in various extratropical regions including the polar regions, which is absent in many previous studies as well as in current CGCMs. Such high extratropical predictability in seasonal precipitation anomalies has a significant seasonality. During JJA (Fig. 8b), the regions with high predictability are primarily located in the extratropical Southern Hemisphere (winter hemisphere), whereas the predictability in the extratropical Northern Hemisphere, particularly in the extensive continental areas, appears to be relatively low. (Cohen et al. 2014; Holland and Bitz 2003; Mccrystall et al. 2021). Similarly, during DJF (Fig. 8d), high predictability appears to be more considerably in the extratropical Northern Hemisphere (winter hemisphere), particularly in Europe, the North Atlantic, and the North Pacific, where TCC values reach and even exceed 0.5. It is inferred that the high seasonal precipitation predictability in the extratropical winter hemispheres is probably due to that there exist more and stronger extratropical climate modes during winter than during summer that are introduced into the reconstruction of the seasonal precipitation anomalies, as described in the optimal combinations of climate modes. During transitional seasons (MAM and SON), the extratropical regions with high predictability determined by climate modes are characterized by a relatively symmetric distribution about two hemispheres, with comparable numbers of climate modes selected for precipitation reconstruction (Fig. 8a and 8c).

The potential predictability of global seasonal precipitation anomalies derived above with the impacts of major large-scale climate modes originating from the tropics as well as the extratropics of two hemispheres provides an upper limit achievable of the predictability if those climate modes are known or perfectly predicted. In fact, those climate modes are unknown or not accurately predicted, thus the predictability is said to be potential. Here we make an analysis by comparing the potential predictability of global seasonal precipitation anomalies identified in this study with their actual skills predicted by 8 state-of-the-art operational CGCMs for C3S. Figure 9 presents the spatial distributions of TCC skills of global seasonal precipitation anomalies reconstructed with the optimal climate mode combinations versus those predicted by the C3S multi-model ensemble (MME) mean for four seasons of 1994–2016, with a globally-averaged value of TCC labeled in each panel. It is evidently seen from Fig. 9 that TCCs for the potential predictability of global seasonal precipitation anomalies determined by climate modes are significantly higher than those by dynamical model predictions, which is particularly pronounced in the extratropical summer hemispheres, i.e., during JJA in the extratropical Northern Hemisphere and DJF in the extratropical Southern Hemisphere, although both TCCs are comparable in the tropics. During boreal summer (JJA), CGCMs exhibit extremely limited predictive skills for seasonal precipitation anomalies in extratropical Northern

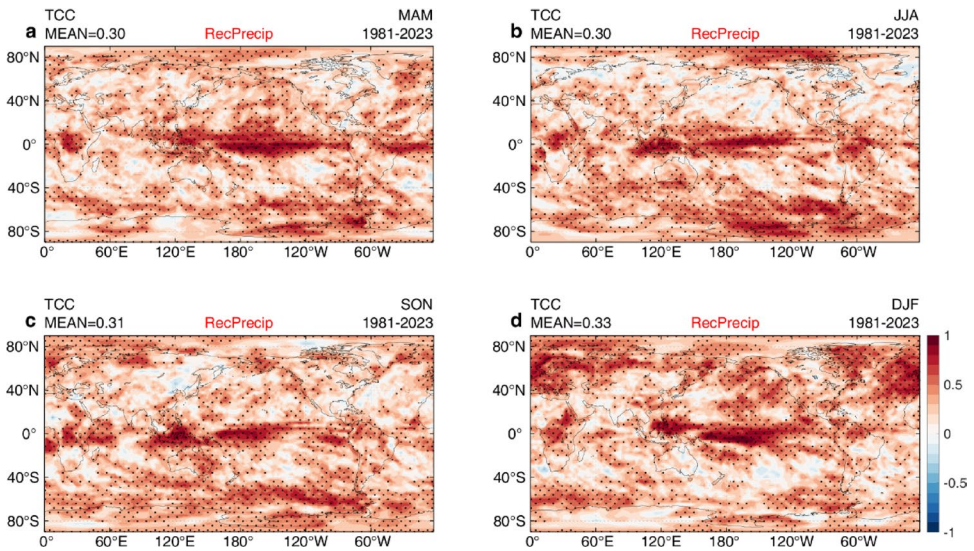

Fig. 8 Spatial distributions of potential predictability of global seasonal precipitation anomalies determined by climate modes, as measured by temporal correlation coefficients (TCCs) between independently-reconstructed and observed seasonal precipitation anomalies for **a** MAM, **b** JJA, **c** SON, and **d** DJF of 1981–2023. Note that the areas with TCC values exceeding 95% confidence level with the Student's *t*-test are stippled

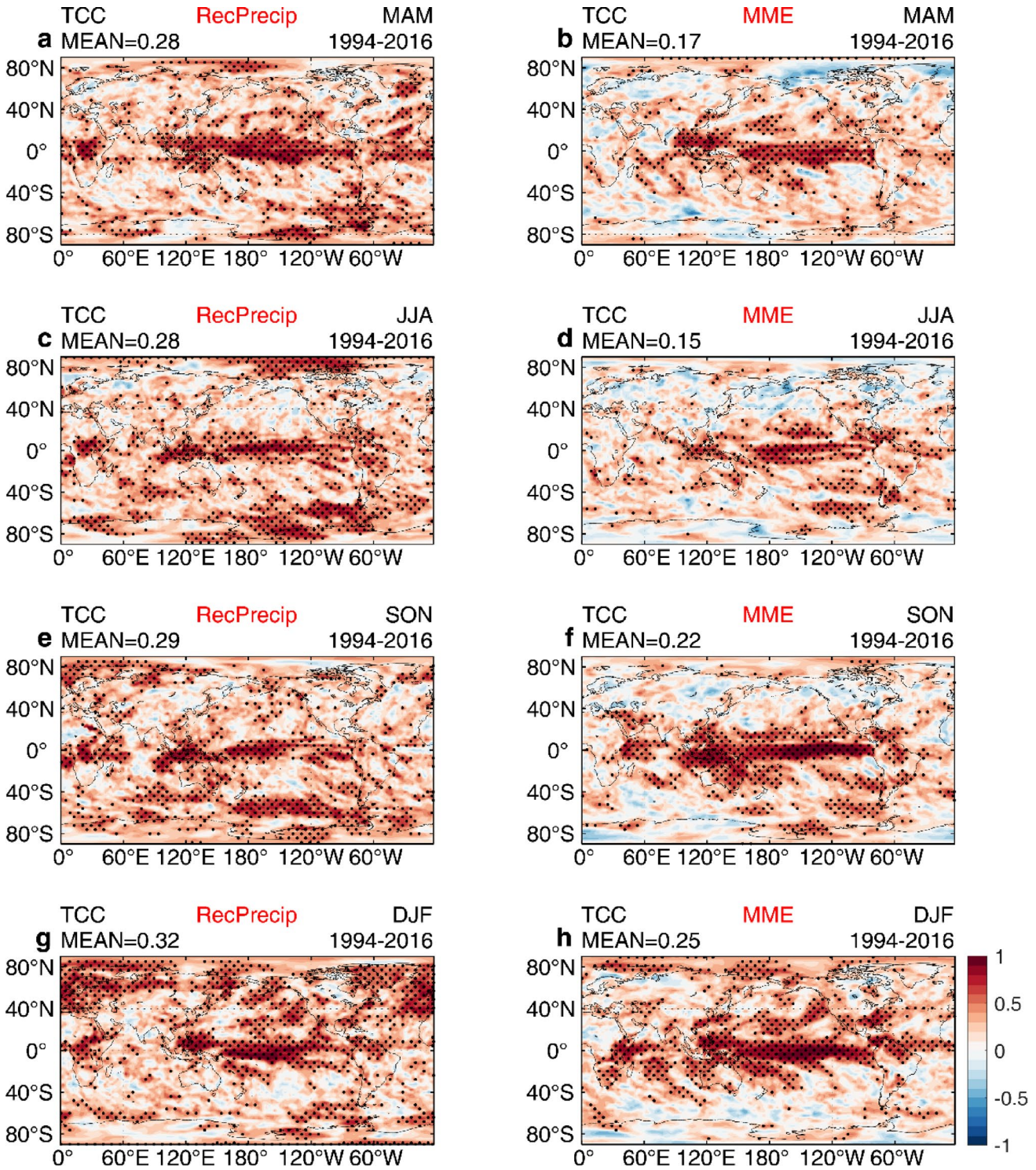

Fig. 9 Spatial distributions of TCC skills of global seasonal precipitation anomalies reconstructed with the optimal climate mode combination (left panels) versus those predicted with one season lead by the C3S multi-model ensemble (MME) mean (right panels) for four seasons of 1994–2016, with a globally-averaged value of TCC labeled in each panel. Note that the areas with TCC values exceeding 95% confidence level with the Student's *t*-test are stippled

Hemisphere, with certain areas even showing negative TCC skills (Fig. 9d), while in the regions the potential predictability determined by climate modes substantially are high (Fig. 9c). During austral summer (DJF), there is a similar situation in the extratropical Southern Hemisphere (Fig. 9h and 9g). Recent studies have shown that the deficiency in predictive skills of seasonal precipitation anomalies is common in current CGCMs (Hausfather et al. 2020; Giuntoli et al. 2022). In terms of our results, we infer that the limited capability of CGCMs in accurately predicting extratropical climate modes is one of the primary reasons for that deficiency. This suggests that improving CGCMs' predictions of the extratropical climate modes is a key for advancing prediction of global seasonal precipitation anomalies in the extratropical regions.

5 Contributions of leading climate modes to the potential predictability

In the last section, we have independently reconstructed the global seasonal precipitation anomalies using optimal combinations of large-scale climate modes, and found that high potential predictability determined by those climate modes exists not only in the tropics but also in many of the extratropical regions, with a globally-averaged TCC up to 0.3 and even more for 1981–2023. In order to further understand the sources of the predictability, here we examine the contributions of leading climate modes to the potential predictability. To achieve this, we employ an approach to assess the contribution of a specific climate mode to the predictability by removing the mode from the independent reconstruction of global seasonal precipitation anomalies with the optimal climate mode combination and looking at the difference between the original TCCs and modified TCCs. Taking DJF as an example, to quantify the contribution of the first tropical climate mode to the predictability, we exclude this mode while retaining the remaining 2 tropical modes, 6 extratropical Northern Hemisphere modes, and 2 extratropical Southern Hemisphere modes, and then calculate TCCs of this modified climate mode combination. Then, the difference between the original TCCs with the optimal climate combination and the modified TCCs with the mode excluded from that combination represents the contribution of the mode to the predictability.

Left panels of Fig. 10 shows the contributions of the first tropical OLR modes (OLR1) to the potential predictability of global seasonal precipitation anomalies for four seasons, as identified with the aforementioned method. It is demonstrated that the modes exert substantial contributions to the high predictability in the tropical regions throughout all seasons, particularly over the Pacific Ocean, the Maritime Continent, the equatorial Indian Ocean, and even the East Asian monsoon regions. As compared to Fig. 8, the contributions of the modes to the tropical predictability are decisive, since the first tropical OLR modes for four seasons are essentially the ENSO signature, as described in Sect. 3 (Fig. 1). To further elucidate the sources of the predictability contributions, we employ regression analysis to present spatial distributions of seasonal precipitation anomalies associated with the first OLR modes, as illustrated in right panels of Fig. 10. As mentioned in Sect. 3, the first OLR modes have almost no interdecadal change, so the regression analysis has been done for the recent 30 years (1991–2020). It can be clearly seen that the spatial distributions of large predictability contributions from the first OLR modes are closely consistent with those of the precipitation anomalies regressed upon the modes. This correspondence is particularly pronounced in the tropics where anomalous convection activities dominate precipitation anomalies, underscoring the critical role of the first OLR modes in shaping precipitation predictability in the tropical regions. In the extratropical areas, the modes also make substantial contributions to the precipitation predictability, especially during DJF, when ENSO exerts significant influences on the precipitation anomalies in southeastern China and southeastern United States (Fig. 10g and h). In the regions characterized by relatively low potential predictability during JJA, such as the continental areas in the Northern Hemisphere, the contributions of the first tropical OLR modes to the predictability are primarily limited to certain Asian monsoon regions, as ENSO can has significant impact on summer precipitation in these regions (Fig. 10c and 10d).

Left panels of Fig. 11 shows the contributions of the first extratropical Southern Hemisphere Z500 modes (Z500S1) which are essentially the AAO modes to the potential predictability of seasonal precipitation anomalies for four seasons. It is demonstrated that the contributions of the modes are primarily concentrated in the extratropical Southern Hemisphere regions, with a significant seasonality. The contributions of the modes to predictability are larger during MAM and JJA (austral winter), but smaller during SON and DJF (austral summer). A comparative analysis of the impacts of the modes on global precipitation anomalies during the recent 30 years (right panels of Fig. 11) reveals a spatial consistency between the regions with large predictability contributions and those with large precipitation anomalies induced by the modes in the extratropical Southern Hemisphere. The notable regions include the southern Africa, the southern Indian Ocean, the southeastern Australia, the southern Pacific, and the southern South America. The modes are stronger during MAM and JJA, which tend to cause larger precipitation anomalies in the extratropical Southern Hemisphere than during other seasons (upper two

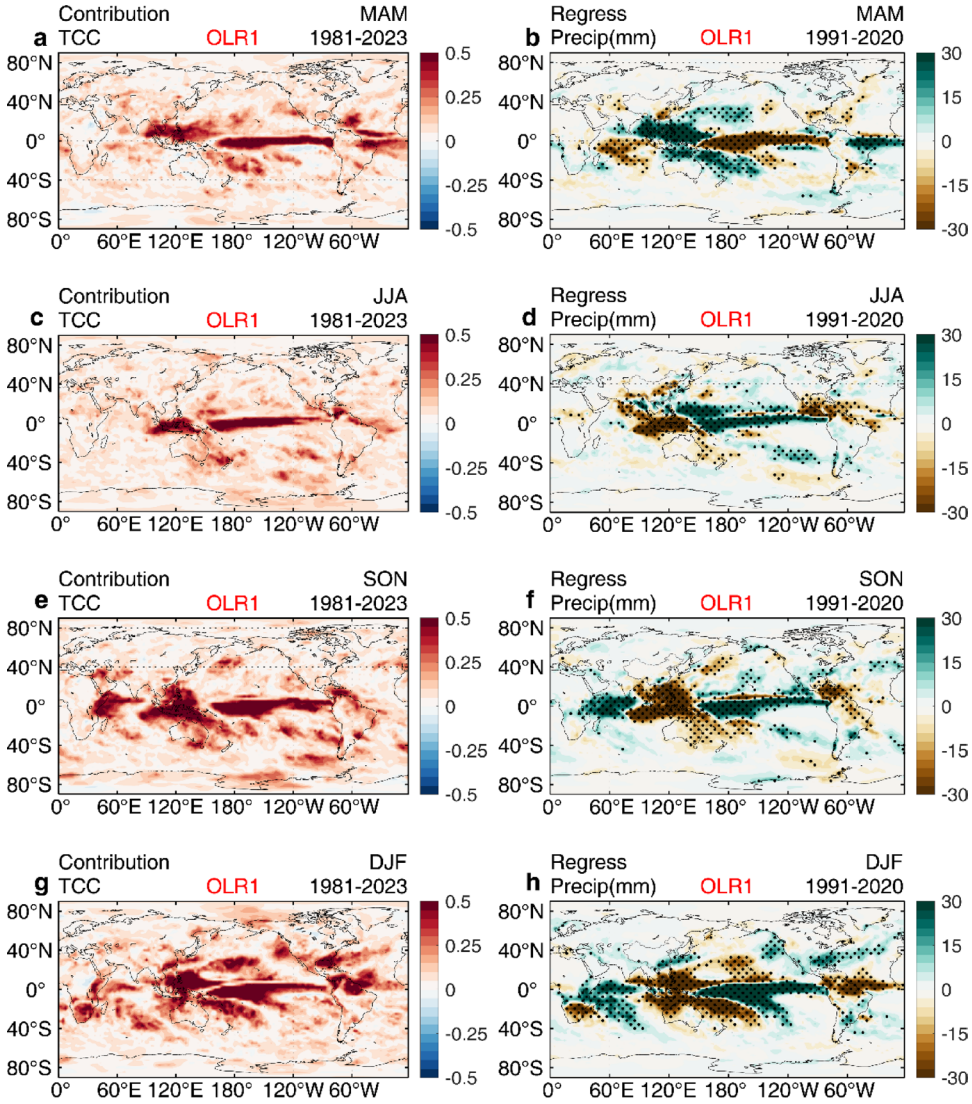

Fig. 10 Spatial distributions of contributions of the first tropical OLR climate modes (OLR1) to the potential predictability of global seasonal precipitation anomalies (left panels) and the global precipitation anomalies (shading, unit: mm) regressed upon these modes for 1991–2020 (right panels) for four seasons. Here, the contribution of a climate mode to the predictability is defined as the difference between the original TCC with the optimal mode combination and the modified TCC with the mode excluded from the combination. Note that the areas with precipitation anomalies in right panels exceeding 95% confidence level with the Student's *t*-test are stippled

panels of Fig. 11), thereby increasing their contributions to the precipitation predictability there during these seasons. However, despite the presence of large precipitation anomalies in the tropics associated with the modes, the contributions of the modes to tropical precipitation predictability are relatively insignificant. This is primarily due to the dominant contributions of tropical climate modes to the tropical precipitation predictability. Furthermore, we notice that the extratropical Southern Hemisphere leading climate modes (AAO) can exert measurable impacts on seasonal precipitation anomalies and contributions to the predictability in the Northern Hemisphere, although those impacts and contributions are weak.

Contributions of the first extratropical Northern Hemisphere Z500 modes (Z500N1) appear to be complex, since those leading modes feature pronounced interdecadal changes as described in Sect. 3 (Fig. 5). Thus, we need to consider interdecadal changes in the contributions of those modes to the potential predictability of global seasonal precipitation anomalies. Left panels of Fig. 12 show the contributions of the first extratropical Northern Hemisphere Z500 modes to the potential predictability of global seasonal precipitation anomalies. It is clearly seen that the modes demonstrate significant contributions to the precipitation predictability in the extratropical Northern Hemisphere regions for all seasons. Notably, during boreal summer (JJA), the leading mode has an exceptionally large contribution to the precipitation predictability in the Arctic and the northern Europe (Fig. 12e). When compared to the results presented in Fig. 8b, it is evident that the leading mode serves as the most important contributor to the potential predictability of summer precipitation anomalies in the Arctic. During winter (DJF), the mode substantially contributes to the precipitation predictability throughout the entire extratropical Northern Hemisphere (Fig. 12m), including the northern Eurasia, the northern North America, the North Pacific, and the

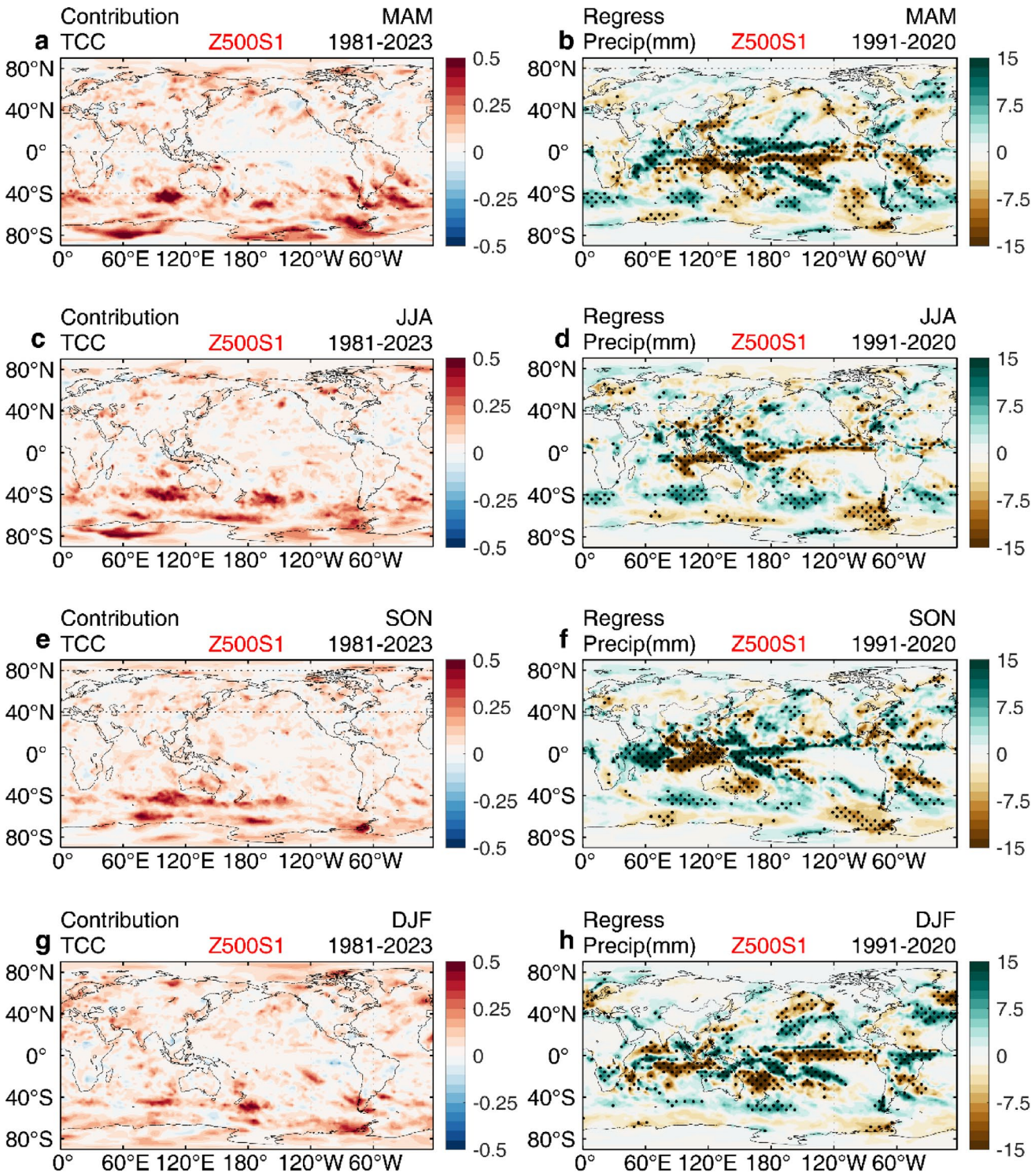

Fig. 11 As in Fig. 10, but for the first extratropical Southern Hemisphere Z500 climate modes (Z500S1)

North Atlantic. During spring (MAM, Fig. 12a) and autumn (SON, Fig. 12i), the modes remain important contributors to the precipitation predictability in the extratropical Northern Hemisphere. Considering the interdecadal changes of the leading modes of four seasons, we analyze impacts of those modes on global seasonal precipitation anomalies in three interdecadal periods (right three columns of Fig. 12) so as to understand the sources of the precipitation predictability in the extratropical Northern Hemisphere. A comparative analysis of the precipitation anomalies associated with

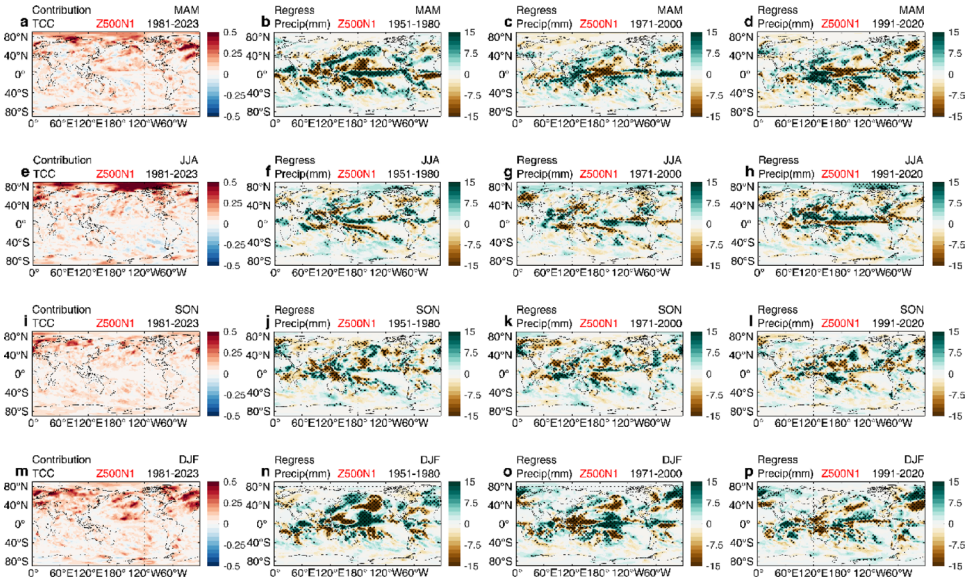

Fig. 12 As in Fig. 10, but for the contributions of the first extratropical Northern Hemisphere Z500 climate mode (Z500N1) to the potential predictability of global seasonal precipitation anomalies (left panels) and the global precipitation anomalies (shading, unit: mm) regressed upon these modes during three interdecadal periods (1951–1980, 1971–2000, and 1991–2020), for four seasons

the leading climate modes during three interdecadal periods demonstrates that the large predictability contributions from the leading modes found in the extratropical Northern Hemisphere, as shown in left panels of Fig. 12, are resulted from the mean effects of the precipitation anomalies induced by the leading climate modes during three interdecadal periods (right three columns of Fig. 12), although the leading mode appears to be different from one period to another, as shown in Fig. 5. For instance, during the first interdecadal period (1951–1980) when the leading climate mode during DJF is characterized by a PNA pattern (Fig. 5d), major precipitation anomalies are located in the North Pacific-North America sector (Fig. 12n), while in the third interdecadal period (1991–2020) when the leading climate mode during DJF is characterized by an NAO pattern (Fig. 5f), major precipitation anomalies shift predominantly to the North Atlantic-Europe region (Fig. 12p). The overlapping contributions from these distinct interdecadal periods results in a spatial distribution of the predictability contributions that spans both the North Pacific-North America and North Atlantic-Europe sectors (Fig. 12m). This finding highlights the advantage and significance of employing a 30-yr sliding window for considering the modulation role of background state changes in leading climate modes, their impacts on the precipitation anomalies, and their contributions to the precipitation predictability.

6 Summary

Global warming has significantly heightened the risk of extreme climate disasters, posing a critical threat to global security and sustainable development. Accurate prediction of global seasonal precipitation is essential for mitigating flood and drought risks. However, current CGCMs still exhibit limited predictability in cross-seasonal prediction of global seasonal precipitation anomalies. Large-scale climate modes play a pivotal role in shaping global seasonal precipitation anomalies and serve as primary sources of seasonal precipitation predictability. Nevertheless, even under the assumption that these climate modes are known or perfectly predicted, the predictability of global seasonal precipitation anomalies determined by these modes remains quantitatively unassessed. This study identifies large-scale climate modes both in the tropics and in the extratropics using two representative variables of tropical OLR anomalies and extratropical Z500 anomalies, and develops a framework with a 30-yr sliding temporal window for reconstructing seasonal precipitation anomalies using contemporaneous climate modes, in order to investigate the potential predictability of global seasonal precipitation anomalies determined by climate modes.

We employ the EOF decomposition method to identify three types of large-scale climate modes from tropical (30°N–30°S) OLR anomalies and extratropical (90°N–30°N and 90°S–30°S) Z500 anomalies in both hemispheres, which represent the dominant large-scale climate signals originating from tropical and extratropical regions, respectively. For recent 30 years, our results show that the tropical leading climate modes for four seasons are consistently characterized by the ENSO signature, while the extratropical Northern Hemisphere leading climate modes primarily appear to the NAO or PNA pattern or their combination, and the extratropical Southern Hemisphere leading climate modes are characterized by the AAO pattern. These climate modes display pronounced seasonality and distinct interdecadal changes. Notably, the extratropical Northern Hemisphere leading mode underwent significant interdecadal shifts

from a PNA pattern during the early period (1951–1980) to an NAO pattern in the latter period (1991–2020). It is important to note that the identified climate modes do not just reflect conventional modes but sometimes are the combinations of the conventional modes.

We develop a framework to independently reconstruct global seasonal precipitation anomalies using those identified climate modes, with a 30-yr sliding temporal window to consider interdecadal changes of climate modes due to the modulation of background state change. By calculating TCC between reconstructed and observed seasonal precipitation anomalies at each grid point, we quantitatively assess the potential predictability of global seasonal precipitation anomalies with the optimal combinations of climate modes for four seasons of 1981–2023. We find that high potential predictability of seasonal precipitation anomalies determined by climate modes exists not only in the tropics, particularly in the tropical Pacific where ENSO as the leading climate mode dominates the predictability, but also in many extratropical regions including the polar areas, with globally-averaged TCCs up to 0.3 and even more for four seasons of 1981–2023. Such high extratropical predictability of seasonal precipitation anomalies has a significant seasonality, with high predictability in the extratropical winter hemispheres (i.e., the extratropical Northern Hemisphere during DJF and the extratropical Southern Hemisphere during JJA), which is attributed to more and stronger extratropical climate modes during local winter than during local summer that determine the extratropical seasonal precipitation anomalies. During boreal winter (DJF), NAO, PNA or their combination as the leading climate modes in different interdecadal periods substantially contribute to high predictability in the extratropical Northern Hemisphere, while during austral winter (JJA), AAO as the leading and dominant climate mode greatly contributes to high predictability in the extratropical Southern Hemisphere.

We consider that the potential predictability of global seasonal precipitation anomalies determined by climate modes derived in this study provides an upper limit achievable of the predictability if those climate modes are known or perfectly predicted. In fact, those climate modes are unknown or not accurately predicted. We compare the potential predictability of global seasonal precipitation anomalies assessed in this study with their hindcast skills predicted by 8 state-of-the-art operational CGCMs of C3S, and find that TCCs for the potential predictability of global seasonal precipitation anomalies determined by climate modes are significantly higher than those by dynamical model predictions, which is particularly pronounced in the extratropical summer hemispheres (i.e., the extratropical Northern Hemisphere during JJA and the extratropical Southern Hemisphere during DJF), although both TCCs are comparable in the tropics. We infer that the deficiency of CGCMs in predictive skills of extratropical seasonal precipitation anomalies is attributed to their limited capability in accurately predicting extratropical climate modes. This suggests that improving CGCMs' predictions of the extratropical climate modes is fundamentally crucial for advancing prediction of global seasonal precipitation anomalies in the extratropical regions. Of course, atmospheric internal chaotic variability in CGCMs is also a factor limiting season precipitation predictability. As the chaotic variability dominates seasonal precipitation anomalies in an extratropical region, improving CGCMs' predictions of the extratropical climate modes may not necessarily advance prediction of seasonal precipitation anomalies in that region.

Acknowledgements This work is jointly supported by the National Key Basic Research & Development Program of China (2022YFE0106600) and the National Natural Science Foundation of China (41621005).

Author contributions All authors contributed to the conception and design of the study. The main idea of the study was put forward by X.-Q.Y. Material preparation, data collection and analysis were performed by Y.W. The manuscript was written by Y.W. and improved by X.-Q.Y., and D.Y. All authors reviewed and approved the final manuscript.

Funding This study is jointly supported by the National Key Basic Research & Development Program of China (2022YFE0106600) and the National Natural Science Foundation of China (41621005).

Data availability The fifth generation ECMWF reanalysis (ERA5) data is available at https://www.ecmwf.int/en/forecasts/dataset/ecmwf-reanalysis-v5. Output data from the 8 state-of-the-art global coupled general circulation models is available from the Copernicus Climate Change Service (C3S) Climate Data Store (CDS) at https://cds.climate.copernicus.eu/datasets and https://doi.org/10.24381/cds.68dd14c3. The data of climate indices is available from NOAA Physical Sciences Laboratory at https://psl.noaa.gov/data/climateindices/list/.

Declarations

Competing interests The authors have no relevant financial or non-financial interests to disclose.

Consent for publication Written informed consent for publication was obtained from all participants.

References

Abram NJ, Gagan MK, Cole JE et al (2008) Recent intensification of tropical climate variability in the Indian Ocean. Nat Geosci 1:849–853. https://doi.org/10.1038/ngeo357

Ashok K, Guan ZY, Yamagata T (2001) Impact of the Indian Ocean dipole on the relationship between the Indian monsoon rainfall and ENSO. Geophys Res Lett 28:4499–4502. https://doi.org/10.1029/2001gl013294

Buontempo C, Burgess SN, Dee D et al (2022) The Copernicus Climate Change Service: climate science in action. Bull Am Meteorol Soc 103:E2669–E2687. https://doi.org/10.1175/Bams-D-21-0315.1

Casanueva A, Rodríguez-Puebla C, Frías MD et al (2014) Variability of extreme precipitation over Europe and its relationships with teleconnection patterns. Hydrol Earth Syst Sci 18:709–725. https://doi.org/10.5194/hess-18-709-2014

Chen SF, Wu RG, Chen W (2020) Strengthened connection between springtime North Atlantic Oscillation and North Atlantic Tripole SST pattern since the late 1980s. J Climate 33:2007–2022. https://doi.org/10.1175/Jcli-D-19-0628.1

Chowdary JS, Patekar D, Srinivas G et al (2019) Impact of the Indo-Western Pacific Ocean capacitor mode on South Asian summer monsoon rainfall. Clim Dyn 53:2327–2338. https://doi.org/10.1007/s00382-019-04850-w

Cohen J, Screen JA, Furtado JC et al (2014) Recent Arctic amplification and extreme mid-latitude weather. Nat Geosci 7:627–637. https://doi.org/10.1038/Ngeo2234

Dai A, Fung IY, Delgenio AD (1997) Surface observed global land precipitation variations during 1900–88. J Climate 10:2943–2962. https://doi.org/10.1175/1520-0442(1997)010%3c2943:SOGLPV%3e2.0.CO;2

Doblas-Reyes FJ, García-Serrano J, Lienert F et al (2013) Seasonal climate predictability and forecasting: status and prospects. Wiley Interdiscip Rev Clim Change 4:245–268. https://doi.org/10.1002/wcc.217

Enomoto T, Hoskins BJ, Matsuda Y (2003) The formation mechanism of the Bonin high in August. Q J R Meteorol Soc 129:157–178. https://doi.org/10.1256/qj.01.211

Feng J, Li J, Li Y (2010) Is there a relationship between the SAM and southwest Western Australian winter rainfall? J Climate 23:6082–6089. https://doi.org/10.1175/2010JCLI3667.1

Gemenne F, Barnett J, Adger WN et al (2014) Climate and security: evidence, emerging risks, and a new agenda. Clim Change 123:1–9. https://doi.org/10.1007/s10584-014-1074-7

Giuntoli I, Fabiano F, Corti S (2022) Seasonal predictability of Mediterranean weather regimes in the Copernicus C3S systems. Clim Dyn 58:2131–2147. https://doi.org/10.1007/s00382-021-05681-4

Gong DY, Ho CH (2003) Arctic oscillation signals in the East Asian summer monsoon. J Geophys Res: Atmos. https://doi.org/10.1029/2002jd002193

Gong DY, Wang SW (1999) Definition of Antarctic Oscillation index. Geophys Res Lett 26:459–462. https://doi.org/10.1029/1999gl900003

Goodrich GB (2007) Influence of the Pacific Decadal Oscillation on winter precipitation and drought during years of neutral ENSO in the western United States. Weather Forecast 22:116–124. https://doi.org/10.1175/Waf983.1

Hassan AS, Yang X-Q, Zao SS (2004) Reproducibility of seasonal ensemble integrations with ECMWF GCM and its association with ENSO. Meteorol Atmos Phys 86:159–172. https://doi.org/10.1007/s00703-003-0024-0

Hausfather Z, Drake HF, Abbott T et al (2020) Evaluating the performance of past climate model projections. Geophys Res Lett. https://doi.org/10.1029/2019gl085378

He SP, Gao YQ, Li F et al (2017) Impact of Arctic Oscillation on the East Asian climate: a review. Earth-Sci Rev 164:48–62. https://doi.org/10.1016/j.earscirev.2016.10.014

Hersbach H, Bell B, Berrisford P et al (2020) The ERA5 global reanalysis. Q J R Meteorol Soc 146:1999–2049. https://doi.org/10.1002/qj.3803

Hobeichi S, Abramowitz G, Sen Gupta A et al (2024) How well do climate modes explain precipitation variability? NPJ Clim Atmos Sci 7:295. https://doi.org/10.1038/s41612-024-00853-5

Holland MM, Bitz CM (2003) Polar amplification of climate change in coupled models. Clim Dyn 21:221–232. https://doi.org/10.1007/s00382-003-0332-6

Hurrell JW, Deser C (2009) North Atlantic climate variability: the role of the North Atlantic Oscillation. J Mar Syst 78:28–41. https://doi.org/10.1016/j.jmarsys.2008.11.026

Ionita M, Vaideanu P, Nichita D et al (2025) Breaking records under clear skies: the impact of sunshine duration and atmospheric dynamics on the 2024 Eastern European extreme summer temperatures. NPJ Nat Hazards 2:82. https://doi.org/10.1038/s44304-025-00137-9

Jan Van Oldenborgh G, Balmaseda MA, Ferranti L et al (2005) Evaluation of atmospheric fields from the ECMWF seasonal forecasts over a 15-year period. J Climate 18:3250–3269. https://doi.org/10.1175/jcli3421.1

Kelley D, Burton C, Di Giuseppe F et al (2025) State of Wildfires 2024-2025. Earth Syst Sci Data 17:5377–5488. https://doi.org/10.5194/essd-17-5377-2025

Kim B-H, Ha K-J (2015) Observed changes of global and western Pacific precipitation associated with global warming SST mode and mega-ENSO SST mode. Clim Dyn 45:3067–3075. https://doi.org/10.1007/s00382-015-2524-2

Le PVV, Randerson JT, Willett R et al (2023) Climate-driven changes in the predictability of seasonal precipitation. Nat Commun 14:3822. https://doi.org/10.1038/s41467-023-39463-9

Lee J-Y, Wang B, Kang IS et al (2010) How are seasonal prediction skills related to models' performance on mean state and annual cycle? Clim Dyn 35:267–283. https://doi.org/10.1007/s00382-010-0857-4

Li T, Wang B, Wu B et al (2017) Theories on formation of an anomalous anticyclone in Western North Pacific during El Nino: a review. J Meteorol Res 31:987–1006. https://doi.org/10.1007/s13351-017-7147-6

Liu ZF, Kennedy CD, Bowen GJ (2011) Pacific/North American teleconnection controls on precipitation isotope ratios across the contiguous United States. Earth Planet Sci Lett 310:319–326. https://doi.org/10.1016/j.epsl.2011.08.037

Liu Y, Sun X, Yang X-Q (2023) Stage-dependent influence of PDO on interdecadal summer precipitation anomalies in eastern China. Clim Dyn 61:2071–2084. https://doi.org/10.1007/s00382-023-06667-0

Lyon B, Barnston AG (2005) ENSO and the spatial extent of interannual precipitation extremes in tropical land areas. J Climate 18:5095–5109. https://doi.org/10.1175/jcli3598.1

Ma MM, Qu YP, Lyu J et al (2022) The 2022 extreme drought in the Yangtze River Basin: characteristics, causes and response strategies. River 1:162–171. https://doi.org/10.1002/rvr2.23

Mccrystall MR, Stroeve J, Serreze M et al (2021) New climate models reveal faster and larger increases in Arctic precipitation than previously projected. Nat Commun 12:6765. https://doi.org/10.1038/s41467-021-27031-y

Mishra N, Prodhomme C, Guemas V (2018) Multi-model skill assessment of seasonal temperature and precipitation forecasts over Europe. Clim Dyn 52:4207–4225. https://doi.org/10.1007/s00382-018-4404-z

Nguyen-Le D, Ngo-Duc T, Matsumoto J (2024) The teleconnection of the two types of ENSO and Indian Ocean Dipole on Southeast Asian autumn rainfall anomalies. Clim Dyn 62:13–23. https://doi.org/10.1007/s00382-024-07163-9

O'reilly CH, Macleod D, Befort DJ et al (2025) Evaluating seasonal forecast improvements over the past two decades. Q J R Meteorol Soc. https://doi.org/10.1002/qj.70036

Palmer TN, Anderson DLT (1994) The prospects for seasonal forecasting - a review paper. Q J R Meteorol Soc 120:755–793. https://doi.org/10.1256/smsqj.51801

Pan LL (2005) Observed positive feedback between the NAO and the North Atlantic SSTA tripole. Geophys Res Lett. https://doi.org/10.1029/2005gl022427

Perkins-Kirkpatrick S, Barriopedro D, Jha R et al (2024) Extreme terrestrial heat in 2023. Nat Rev Earth Environ 5:244–246. https://doi.org/10.1038/s43017-024-00536-y

Piskala V, Huth R (2025) Tracing shifts: interdecadal variations of NAO and PNA patterns from the nineteenth century across multiple reanalyses. J Climate 38:1521–1533. https://doi.org/10.1175/Jcli-D-24-0037.1

Qiu Y, Cai W, Guo X et al (2014) The asymmetric influence of the positive and negative IOD events on China's rainfall. Sci Rep 4:4943. https://doi.org/10.1038/srep04943

Ropelewski CF, Halpert MS (1987) Global and regional scale precipitation patterns associated with the El Niño/Southern Oscillation. Mon Weather Rev 115:1606–1626. https://doi.org/10.1175/1520-0493(1987)115%3c1606:GARSPP%3e2.0.CO;2

Roy T, He XG, Lin PR et al (2020) Global evaluation of seasonal precipitation and temperature forecasts from NMME. J Hydrometeorol 21:2473–2486. https://doi.org/10.1175/Jhm-D-19-0095.1

Saji NH, Goswami BN, Vinayachandran PN et al (1999) A dipole mode in the tropical Indian Ocean. Nature 401:360–363. https://doi.org/10.1038/43854

Seager R, Liu HB, Kushnir Y et al (2020) Mechanisms of winter precipitation variability in the European-Mediterranean region associated with the North Atlantic Oscillation. J Clim 33:7179–7196. https://doi.org/10.1175/Jcli-D-20-0011.1

Shaman J (2014) The seasonal effects of ENSO on European precipitation: observational analysis. J Clim 27:6423–6438. https://doi.org/10.1175/Jcli-D-14-00008.1

Straus DM, Shukla J (2002) Does ENSO force the PNA? J Clim 15:2340–2358. https://doi.org/10.1175/1520-0442(2002)015%3c2340:DEFTP%3e2.0.CO;2

Sun LY, Yang X-Q, Tao LF et al (2021) Changing impact of ENSO events on the following summer rainfall in eastern China since the 1950s. J Climate 34:8105–8123. https://doi.org/10.1175/Jcli-D-21-0018.1

Wang B, Lee JY, Xiang BQ (2015) Asian summer monsoon rainfall predictability: a predictable mode analysis. Clim Dyn 44:61–74. https://doi.org/10.1007/s00382-014-2218-1

Weng HY, Wu GX, Liu YM et al (2011) Anomalous summer climate in China influenced by the tropical Indo-Pacific Oceans. Clim Dyn 36:769–782. https://doi.org/10.1007/s00382-009-0658-9

Wu Z, Wang B, Li J et al (2009a) An empirical seasonal prediction model of the east Asian summer monsoon using ENSO and NAO. J Geophys Res: Atmos. https://doi.org/10.1029/2009jd011733

Wu Z, Li J, Wang B et al (2009b) Can the Southern Hemisphere annular mode affect China winter monsoon? J Geophys Res Atmos. https://doi.org/10.1029/2008jd011501

Xie SP, Hu KM, Hafner J et al (2009) Indian Ocean capacitor effect on Indo-Western Pacific climate during the summer following El Nino. J Climate 22:730–747. https://doi.org/10.1175/2008jcli2544.1

Xie SP, Kosaka Y, Du Y et al (2016) Indo-western Pacific Ocean capacitor and coherent climate anomalies in post-ENSO summer: a review. Adv Atmos Sci 33:411–432. https://doi.org/10.1007/s00376-015-5192-6

Yang X-Q, Anderson JL, Stern WF (1998) Reproducible forced modes in AGCM ensemble integrations and potential predictability of atmospheric seasonal variations in the extratropics. J Climate 11:2942–2959. https://doi.org/10.1175/1520-0442(1998)011%3c2942:RFMIAE%3e2.0.CO;2

Yang D, Yang XQ, Xie Q, Zhang Y, Ren X, Tang Y (2016) Probabilistic versus deterministic skill in predicting the western North Pacific-East Asian summer monsoon variability with multimodel ensembles. J Geophys Res Atmos 121:1079–1103. https://doi.org/10.1002/2015JD023781

Yang D, Yang X-Q, Ye D, Sun X, Fang J, Chu C, Feng T, Jiang Y, Liang J, Ren X, Zhang Y, Tang Y (2018) On the relationship between probabilistic and deterministic skills in dynamical seasonal climate prediction. J Geophys Res Atmos 123:5261–5283. https://doi.org/10.1029/2017JD028002

Yang DJ, Tang YM, Yang X-Q et al (2021) A theoretical relationship between probabilistic relative operating characteristic skill and deterministic correlation skill in dynamical seasonal climate prediction. Clim Dyn 56:3909–3932. https://doi.org/10.1007/s00382-021-05678-z

Yang D, Tang Y, Yang X-Q, Song X, Tan X, Wu Y, Yan X, Liu T, Sun X (2023) Probabilistic versus deterministic potential seasonal climate predictability under the perfect-model framework. Clim Dyn 61:4429–4447. https://doi.org/10.1007/s00382-023-06814-7

Yuan Y, Yang H, Zhou W et al (2008) Influences of the Indian Ocean dipole on the Asian summer monsoon in the following year. Int J Climatol 28:1849–1859. https://doi.org/10.1002/joc.1678

Zhang LX, Zhou TJ, Zhang X et al (2024) Attribution of the extreme 2022 summer drought along the Yangtze River Valley in China based on detection and attribution system of Chinese Academy of Sciences from. Bull Am Meteorol Soc 105:1062–1067. https://doi.org/10.1175/Bams-D-23-0258.1

Zhang WX, Zhou TJ, Ye WH et al (2025) A year marked by extreme precipitation and floods: weather and climate extremes in 2024. Adv Atmos Sci 42:1045–1063. https://doi.org/10.1007/s00376-025-4540-4

Zhou ZQ, Xie SP, Zhang R (2021) Historic Yangtze flooding of 2020 tied to extreme Indian Ocean conditions. Proc Natl Acad Sci U S A 118:e2022255118. https://doi.org/10.1073/pnas.2022255118

Zhou BT, Guo C, Hu YP et al (2025) Enhanced influence of the North Atlantic Oscillation on winter snowfall in northern China since 2000. Sci China Earth Sci 68:1236–1244. https://doi.org/10.1007/s11430-024-1516-9

Zhu YM, Yang X-Q, Xie Q et al (2008) Covarying modes of the Pacific SST and northern hemispheric midlatitude atmospheric circulation anomalies during winter. Prog Nat Sci-Mater Int 18:1261–1270. https://doi.org/10.1016/j.pnsc.2008.05.005